

Accurate Machine Learning Predictions of Coercivity in High-Performance Permanent Magnets

Churna Bhandari,^{1,*} Gavin N. Nop,^{1,2} Jonathan D.H. Smith,^{1,2} and Durga Paudyal^{1,3}

¹The Ames National Laboratory, U.S. Department of Energy, Iowa State University, Ames, Iowa 50011, USA

²Department of Mathematics, Iowa State University, Ames, Iowa 50011, USA

³Department of Electrical and Computer Engineering, Iowa State University, Ames, Iowa 50011, USA

(Dated: December 24, 2023)

Increased demand for high-performance permanent magnets in the electric vehicle and wind turbine industries has prompted the search for cost-effective alternatives. Discovering new magnetic materials with the desired intrinsic and extrinsic permanent magnet properties presents a significant challenge to researchers because of issues with the global supply of rare-earth elements, material stability, and a low maximum magnetic energy product BH_{max} . While first-principle density functional theory (DFT) predicts materials' magnetic moments, magneto-crystalline anisotropy constants, and exchange interactions, it cannot compute extrinsic properties such as coercivity (H_c). Although it is possible to calculate H_c theoretically with micromagnetic simulations, the predicted value is larger than the experiment by almost an order of magnitude, due to the Brown paradox. To circumvent these issues, we employ machine learning (ML) methods on an extensive database obtained from experiments, DFT calculations, and micromagnetic modeling. The use of a large experimental dataset enables realistic H_c predictions for materials such as Ce-doped $\text{Nd}_2\text{Fe}_{14}\text{B}$, comparing favorably against micromagnetically simulated coercivities. Remarkably, our ML model accurately identifies uniaxial magneto-crystalline anisotropy as the primary contributor to H_c . With DFT calculations, we predict the Nd-site dependent magnetic anisotropy behavior in $\text{Nd}_2\text{Fe}_{14}\text{B}$, confirming that Nd $4g$ -sites mainly contribute to uniaxial magneto-crystalline anisotropy, and also calculate the Curie temperature (T_C). Both calculated results are in good agreement with experiment. The coupled experimental dataset and ML modeling with DFT input predict H_c with far greater accuracy and speed than was previously possible using micromagnetic modeling. Further, we reverse-engineer the grain-boundary and inter-grain exchange coupling with micromagnetic simulations by employing the ML predictions.

I. INTRODUCTION

With the rapid advance of computational capabilities, there is considerable research interest in machine learning (ML) methods for predicting material properties using extensive databases^{1,2}. Of specific interest is the remarkable speed of these techniques, which outperform traditional first-principle methods like density functional theory (DFT) by an order of magnitude. ML methods can deal with complex structures, and are desirable for discovering high-performance permanent magnet materials much needed for the electric vehicle and wind turbine industries. Although recent advances in first-principle methods such as DFT have enabled successful prediction of intrinsic properties, e.g., magnetic moments, magneto-crystalline anisotropy, and exchange interactions, the prediction of coercivity (H_c) is a daunting task. Theoretically, H_c can be computed by solving the phenomenological Landau–Lifshitz–Gilbert equation (LLGE) with micromagnetic simulations, but these simulations overestimate the experimental H_c by an order of magnitude due to the Brown paradox^{3–5}. Previous papers employing ML to predict the extrinsic properties^{6–9} have been limited exclusively to micromagnetically simulated materials.

ML requires datasets that include information about material properties such as crystal structure, micromagnetic grain size and boundaries, saturation magnetization (M_s), the uniaxial magnetocrystalline anisotropy constant (K_u), the exchange stiffness constant (A_{ex}), and the Curie temperature (T_C). To build predictive models based on our dataset, we utilize classical ML and artificial neural network (ANN) algorithms^{10–12}. These models establish patterns and relationships between the independent and dependent (H_c) material properties. They are trained on subsets of the known data and tested on the complementary subsets to assess model accuracy and reliability.

An extensive survey of the literature resulted in a dataset of 300 experimentally known materials (see Supplementary¹³ Table I), to our knowledge the largest current experimental ML magnetic dataset. Our second dataset consists of 8770 micromagnetically computed permanent magnet materials. Various predictive techniques, including ML, statistical inference, and micromagnetic modeling (mumax³ program) are applied to both datasets to predict and compare H_c ^{14,15}. In experimental materials, we find standard non-linear models such as the decision tree (DT), extreme gradient boosting (XGB), and random forest (RF)¹⁶ produce excellent results with $R^2 \sim 0.87$ (where R^2 is a standard statistical measure of accuracy in regression), but tuning the XGB regressor improves the R^2 measure to 0.89. Most importantly, ML

* cbb@ameslab.gov

clearly demonstrates that H_c is related directly to K_u , weakly to A_{ex} , and inversely to M_s .

We predict the H_c of cerium (Ce)-doped $\text{Nd}_2\text{Fe}_{14}\text{B}$ 2:14:1 materials to demonstrate the complete pipeline enabled by the new ML toolkit coupled with *ab initio* calculations. First, for a pure neo-magnet, the site contribution to magnetocrystalline anisotropy is analyzed with DFT calculations showing that 4*g*-sites mainly contribute to the uniaxial magneto-crystalline anisotropy. Second, our computed T_C for a pure compound using Green's function in the atomic sphere approximation (ASA) is in good agreement with experiment. Finally, we employ DFT-computed parameters in ML for predicting the H_c of Ce-doped compositions. The ML-predicted H_c matches with experiment, demonstrating that the *ab initio* computed input parameters and the ML methodology are sufficient to predict experimental H_c , even without access to experimental conditions and advanced internal structural properties. Conversely, the ML prediction for selected candidate materials is used to engineer their grain boundary size (GBS) and inter-grain coupling.

II. MICROMAGNETISM

Micromagnetics is the study of the behavior of magnetic materials typically in the nanometer range. During its early formulation^{17,18}, the field emphasized qualitative aspects of magnetism: the role of domain structures, domain walls, and magnetic vortices in ferromagnetic materials. The transition to computer simulation in micromagnetics was a significant advance, providing detailed examination of the forces at play inside a magnetic material¹⁹.

Naively, the estimate $\frac{2K_u}{M_s}$ gives an upper bound on H_c ^{3,20}. However, this estimate disregards impurities and multi-grain structures in materials, leading to a gross overestimate of H_c from theory alone: the Brown paradox. Micromagnetic simulations which include demagnetization (shape anisotropy) are crucial for a good understanding of magnetic materials, but the interplay among these complex effects and the Brown paradox still hinder accurate predictions of H_c .

A. Theory

Magnetodynamics is described by a nonlinear partial differential equation for the spatio-temporal magnetization vector $\mathbf{M}(\mathbf{r}, t)$. The time evolution of $\mathbf{M}(\mathbf{r}, t)$ is given by a phenomenological Landau-Lifshitz-Gilbert (LLG) equation^{17,18}

$$\frac{\partial \mathbf{M}(\mathbf{r}, t)}{\partial t} = \frac{\gamma}{1 + \alpha^2} \mathbf{M}(\mathbf{r}, t) \times \mathbf{H}_{\text{eff}}(\mathbf{r}, t) - \frac{\alpha\gamma}{1 + \alpha^2} \mathbf{M}(\mathbf{r}, t) \times [\mathbf{M}(\mathbf{r}, t) \times \mathbf{H}_{\text{eff}}(\mathbf{r}, t)] \mathbf{1}$$

Here, $\mathbf{M}(\mathbf{r}, t)$ is the unit vector describing the magnetization of the material with M_s as the saturation magnetic moment per unit volume, while $\mathbf{H}_{\text{eff}}(\mathbf{r}, t)$, γ , and α respectively are the effective static magnetic field, the gyromagnetic ratio, and the damping parameter (quantifying the rate at which the magnetization relaxes back to equilibrium). In Eq. (1), the first term is the precession of the magnetic moment around the external magnetic field. The second term is the damping, which relaxes the magnetic moment to the equilibrium. For time-independent scenarios, such as the computation of a hysteresis loop, the α term is set to 0. Then, $\mathbf{H}_{\text{eff}} = \mathbf{H} + \mathbf{H}_{\text{ms}} + \mathbf{H}_{\text{ex}} + \mathbf{H}_{\mathbf{a}}$. The terms are as follows. \mathbf{H} is the externally applied field, which is taken as a parameter. \mathbf{H}_{ms} is a long-range magnetic field

$$\mathbf{H}_{\text{ms}}(\mathbf{r}) = \frac{1}{4\pi} \int \nabla \nabla' \frac{1}{|\mathbf{r} - \mathbf{r}'|} \cdot \mathbf{M}(\mathbf{r}') d\mathbf{r}' \quad (2)$$

corresponding to self-interaction of the induced magnetic field with the magnetization across the material²¹. The exchange field is the Laplacian of the magnetization, which is obtained from the classical Heisenberg model

$$\mathbf{H}_{\text{ex}} = \frac{2A_{\text{ex}}}{M_s} \nabla \mathbf{M}(\mathbf{r}, t). \quad (3)$$

Although this expression was originally deduced for localized spins, it is still valid for itinerant systems to the first order approximation. A_{ex} is a measure of the strength of magnetic exchange interaction. $H_{\mathbf{a}}$ is the uniaxial anisotropy term, written as

$$\mathbf{H}_{\mathbf{a}} = \frac{2K_{u1}}{M_s} (\mathbf{u} \cdot \mathbf{M}(\mathbf{r}, t)) \mathbf{u} + \frac{2K_{u2}}{M_s} (\mathbf{u} \cdot \mathbf{M}(\mathbf{r}, t))^3 \mathbf{u} \quad (4)$$

where K_{u1} and K_{u2} are anisotropy constants, and u indicates the direction of the anisotropy vector, making it easier for the magnetization to align with the direction of u in the case of ferromagnetic materials. Most papers only envisage a single constant: $K_{u1} = K_u$ and $K_{u2} = 0$. Other terms, such as the Dzyaloshinskii-Moriya interaction (DMI), were neglected due to the lack of experimental data for current materials and the relatively weak effect in modern magnetic materials²².

In order to estimate fundamental magnetic parameters in cases of partial experimental information, the following relations were utilized. A_{ex} is inversely proportional to the lattice constant (a) as given by

$$A_{\text{ex}} = \frac{JS^2}{a} n, \quad (5)$$

where S is the spin quantum number, and n is the number of magnetic ions per unit cell. Equivalently, A_{ex} can be expressed approximately in terms of T_C as

$$A_{\text{ex}} \sim \frac{3T_C}{2za}. \quad (6)$$

Here z is the number of the nearest neighbors of a magnetic ion. Finally, the equation

$$BH_{\text{max}} = \frac{\mu_0 M_s^2}{4} \quad (7)$$

is used to estimate M_s from the vacuum permeability μ_0 and the maximum energy product BH_{\max} , which is given by the maximum product of the magnetic flux density and the magnetic field strength at any point on the hysteresis loop²³.

The micromagnetic equations are solved in the continuum approximation $\mathbf{M}(\mathbf{r}, t) = M_s(r)\mathbf{m}(\mathbf{r}, t)$ ^{24–26}. \mathbf{H}_{eff} is deduced from the magnetic free energy functional $F[\mathbf{m}]$ as $\mathbf{H}_{\text{eff}} = -\frac{1}{\mu_0 M_s} \frac{\delta F[\mathbf{m}]}{\delta \mathbf{m}}$;

$$F[\mathbf{m}] = \int_V \left[A_{ex}(\nabla \mathbf{m})^2 - \mu_0 \mathbf{M} \cdot \mathbf{H}_{\text{ex}} - K_u(\mathbf{m} \cdot \mathbf{u})^2 - \mu_0 \mathbf{M} \cdot \mathbf{H} - \frac{\mu_0}{2} \mathbf{M} \cdot \mathbf{H}_{\text{dem}} + f_{\text{DMI}}(\mathbf{m}) + \dots \right] d^3 \mathbf{r}, \quad (8)$$

where f_{DMI} is DMI. Additional terms may be added as needed to count for additional interactions. The $F[m]$ is minimized with respect to m using the steepest descent algorithm as implemented in the micromagnetic program²⁶. Then the hysteresis loop is obtained by evaluating m in each equilibrium magnetic state for different values of the external applied magnetic field.

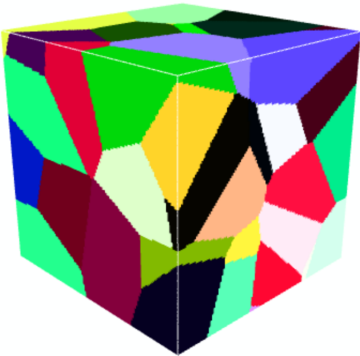


FIG. 1. A magnetic cuboid of size $128 \times 128 \times 128 \text{ nm}^3$ showing different micromagnetic grains. The colors within each grain refer to different magnetization directions. The snapshot of spin texture is captured during the micromagnetic simulation.

B. Experimental materials

An experimental database of 300 magnetic materials was assembled^{20,27–81}. A material was chosen if K_u , M_s , and H_c were explicitly included in the experimental results. For the $\text{R}_2\text{Fe}_{14}\text{B}$ family (where R is a rare-earth element) and some other materials, only the experimental anisotropy field (H_a) is available, so the estimate $H_c \sim H_a/4$ was used⁸².

The exchange strength A_{ex} was determined in one of three different ways. The first was a direct reporting of the stiffness exchange, which was rarely available. For some materials, the value was interpolated from the values for similar alloys and compounds. The third method derived A_{ex} from the

Curie-stiffness relation in Eq. (6), using the experimental Curie temperature T_C and known lattice constant a ⁸³. This latter method was used for $\text{R}_2\text{Fe}_{14}\text{B}$, including Ce-doped $\text{Nd}_2\text{Fe}_{14}\text{B}$ ⁷¹, binary alloys⁶⁹, SmCo_5 , 1:5 compositions⁶⁶, La/Pr/Co-doped hexaferrites⁶¹, and other element doped hexaferrites^{56,57,60,84}.

There was significant variation in the reported H_c values, depending on the experimental conditions and fabrication methods. For example, the atmospheric composition during the annealing of iron (Fe) magnets affected H_c as oxygen modified the material composition during the hardening process. Oxygenated crystalline defects, such as nucleation and pinning of the domain walls, play critical roles in the H_c mechanism. The nucleation field⁸⁵ (the magnetic field at which the atomic spin ceases to align along the magnetic easy axis) lowers the measured H_c , while pinning does the opposite.

Cooling rates have significant effects on the material grain size^{20,27–81}. Several dozen materials (most notably Nd and Fe based ferromagnets) do have grain size recorded in the database. Grain composition, as visualized in Fig. 1, is known to be heavily predictive of a material's H_c ⁸⁶. However, correlating the grain measurements from different sources made it apparent that a single number cannot completely represent the grain structure, and that the particular measurement techniques employed may induce additional inaccuracies. In any material with multiple measurements for a property, a representative median was selected from a specific experiment (defaulting to papers with more comprehensive materials property estimates). This choice was made before the application of statistical techniques, to ensure that no bias contaminated the dataset.

For the better training of ML networks, an additional supplementary database was computed, using micromagnetic modeling with H_{ms} , H_{ex} , H , H_{dem} , and H_a in the H_{eff} . Using the uniaxial approximation, A_{ex} , K_u , and M_s were supplied as the inputs for stiffness exchange, magnetocrystalline anisotropy, and saturation magnetization. The input parameters were uniformly sampled from the cuboid determined by the ranges of A_{ex} , K_u , and M_s in the 300 experimental materials. There are then two measures of H_c : the experimentally measured coercivity $H_c(\text{exp})$, possessed only by the experimental materials, and the computationally determined H_c , calculated for both the hypothetical and the experimental materials.

For micromagnetic modeling, simple structures were chosen for the magnetic samples. Due to the limited grain structure data, for the majority of the database a single structure composed of multiple grains would have been chosen for the materials. This would have induced scaling on the H_c , which instead may be modeled directly with ML. As no grains or boundaries were involved in the computation, a magnetic cube of $32 \times 32 \times 32 \text{ nm}^3$ scale was found to be sufficient to avoid loss of precision in the uniform uniaxial anisotropy alignment. For Ce-substituted compositions, we used simulation cells of size

$128 \times 128 \times 128 \text{ nm}^3$ for grain boundary engineering as shown in Fig. 1.

C. Micromagnetic results

We compute the H_c for experimentally known systems, and list the comparison of the calculated and experimental values for selected materials in Table I. Theoretically, the upper limit for H_c is the anisotropy field⁸⁷ $H_a = \frac{2K_u}{M_s}$; however, the true experimental value is an order of magnitude smaller due to the uncertainty in the coercivity mechanism in permanent magnets, commonly known as the Brown paradox³. Experimentally measured H_c values fit well with the empirical Kronmüller equation⁸⁸ $H_c = cH_a - N_{\text{eff}}4\pi M_s$ ^{89,90}, where cH_a is the field to nucleate a reverse domain, and $N_{\text{eff}}4\pi M_s$ is the demagnetization field, with c and N_{eff} being renormalization factors. For example, $\text{Nd}_2\text{Fe}_{14}\text{B}$ (sintered) has $c \sim 0.25(0.37)$ and $N_{\text{eff}} \sim 0.26(1)$.^{89,90}

The micromagnetically simulated H_c values differ from the experimental values by a factor of up to ~ 5 . Interestingly, these values are very similar to the experimental H_a . Moreover, for some materials, the use of the estimated values for M_s , A_{ex} , and K_u using the empirical relations as discussed in Eqs. (5)–(7) will result in additional error. In general, H_c depends non-linearly on grain size and domain wall width or particle size in magnetic materials^{91–95}. In modern manufacturing, grain sizes are larger relative to domain sizes. This is especially common in neo-magnets, leading to a decrease of H_c with increasing grain size⁹⁶, where higher grain surface area hosts more defects. Grain boundary size also affects the demagnetization factor⁹⁷, further reducing H_c .

The experimental features for 211 of the 300 materials in the dataset are known, while the remaining 90 materials require the use of the aforementioned theoretical models to determine A_{ex} from experimental results. These materials show larger discrepancies in the micromagnetically predicted H_c , which is worth investigating both experimentally and theoretically. We show a comparison of these results (for selected key magnetic materials) in Table I. As all micromagnetically predicted H_c values are overestimated, the only meaningful comparison is obtained with a scaled coercivity cH_c , which for $c = 0.25$ fits well with the experimental values obtained for the 210 materials. The cH_c estimate is generally a good match for 2:14:1 compositions, except for Co-based $\text{Nd}_2\text{Co}_{14}\text{B}$ and $\text{Gd}_2\text{Co}_{14}\text{B}$. However, the appropriate scaling factor may vary for different compositions. Overall, the H_c variation with independent features is similar in both theory and experiment, although there are some exceptions such as $\text{La}_2\text{Fe}_{14}\text{B}$. For 1:5 compositions, a similar trend is evident.

III. MACHINE LEARNING

A. Classical machine learning algorithms

Machine learning (ML) encompasses a variety of advanced statistical techniques. It creates a correspondence between a space of independent variables, X , and a space of dependent variables, Y , by taking a ground truth function $f_o : X_o \rightarrow Y$ representing a sequence of observations on a limited subset $X_o \subset X$ of the data to construct a more general function $f : X \rightarrow Y$ which extends the function f_o . This ground truth function may also be represented as a list of observations $\{x_i \mapsto y_i\}_i \subset X_o \times Y$. The method by which f is constructed from f_o is referred to as ML, and it is written symbolically as $f = ML(f_o) = ML(\{x_i \mapsto y_i\}_i)$, where ML is optionally subscripted to indicate the algorithm or hyperparameters in use.

The goal of ML is to represent the structure underlying f_o as f . This is usually quantified by splitting the observations into a training set f'_o and testing set f_o^* so that $f'_o \cap f_o^* = \emptyset$. Then the function is constructed relative to a norm, termed a loss function, so that $\|f'_o - ML(f'_o)\|$ is minimized in some appropriately defined subspace of $X \rightarrow Y$ to avoid overfitting. The quality of the fit with $f = ML(f'_o)$ is measured by evaluating $\|f_o^* - f\|$ using the same class of norms. In this paper, all ML algorithms use the standard Euclidean norm.

We use the `scikit-learn` library for the Python programming language for predictive data analysis⁹⁸. The dataset (both experimental and theoretical) is split into a 70:30 train-to-test data set ratio for the model training. Performance does not change drastically by modifying the split ratio to 80:20. The classical linear ML models used are:

1. Linear regression;
2. Lasso regularization;
3. Ridge regularization.

The non-linear classical ML models used are:

1. Decision tree (DT) regression;
2. Random forest (RF) regression;
3. Gradient boost (GB) regression;
4. XGBoost (XGB) regression.

In ML training with cross-validation, the training dataset is further divided into two parts - the training and the validation datasets. Most ML models have arbitrary hyperparameters, which are not modified directly during training. The validation dataset allows a meta-training of the ML models by random or grid search on the training data and evaluation on the validation set without contaminating the testing set by predicting an ML hyperparameter choice for test set evaluation. The most

TABLE I. Comparison of calculated and experimental H_c for different rare-earth permanent magnets. For realistic comparisons, the mumax^3 values are scaled by a factor of $c = 0.25$ in column cH_c . The H_c^{diff} column presents the difference between cH_c and H_c^{exp} .

Material	M_s^{exp} (MA/m)	A_{ex}^{exp} (pJ/m)	K_u^{exp} (MJ/m ³)	H_c^{exp} (T)	$H_c^{\text{mumax}^3}$ (T)	cH_c (T)	H_c^{diff} (T)
La ₂ Fe ₁₄ B	1.09	7.41	1.4	0.50	2.11	0.53	0.03
Ce ₂ Fe ₁₄ B	0.93	6.00	1.70	0.54	3.14	0.79	0.25
Pr ₂ Fe ₁₄ B	1.24	7.94	4.66	1.54	6.46	1.62	0.08
Nd ₂ Fe ₁₄ B	1.27	8.23	4.65	1.24	6.25	1.56	0.32
Gd ₂ Fe ₁₄ B	0.71	9.33	0.85	0.23	2.40	0.60	0.37
Tb ₂ Fe ₁₄ B	0.56	8.78	6.13	2.93	21.62	5.41	2.48
Dy ₂ Fe ₁₄ B	0.56	9.42	4.24	1.70	14.79	3.70	1.99
Ho ₂ Fe ₁₄ B	0.64	8.14	2.42	0.75	7.26	1.82	1.07
Lu ₂ Fe ₁₄ B	0.93	7.66	1.21	0.29	2.30	0.58	0.28
Y ₂ Fe ₁₄ B	1.12	8.01	1.46	0.19	2.16	0.54	0.35
Th ₂ Fe ₁₄ B	1.12	6.77	1.46	0.17	2.10	0.53	0.36
La ₂ Co ₁₄ B	0.79	1.50	1.19	0.34	3.06	0.77	0.42
Pr ₂ Co ₁₄ B	1.04	1.51	5.20	2.50	9.43	2.36	-0.14
Nd ₂ Co ₁₄ B	1.08	1.51	2.42	3.69	4.22	1.05	-2.64
Gd ₂ Co ₁₄ B	0.23	1.52	1.03	0.30	9.48	2.37	2.07
Y ₂ Co ₁₄ B	0.85	1.52	1.19	0.34	2.84	0.71	0.37
SmCo ₅	0.86	1.20	1.72	7.50	38.80	9.70	2.20
YCo ₅	0.78	7.11	5.50	3.90	13.33	3.33	-0.57
LaCo ₅	0.71	6.47	6.30	5.25	16.89	4.22	-1.03
CeCo ₅	0.60	5.13	6.40	5.70	20.66	5.17	0.57
PrCo ₅	0.94	6.96	8.10	5.32	16.08	4.02	-1.30
NdCo ₅	0.93	7.09	0.24	0.15	0.47	0.12	-0.03

relevant cross-validation method is k-fold validation. The dataset is randomly split into k disjoint subsets, then one set is chosen as the validation dataset, while the others are chosen as training datasets.

B. Artificial neural networks

An artificial neural network (ANN) is suitable for high complexity problems such as H_c prediction. Fig. 2 shows a schematic diagram (a portion used in the calculations) for an ANN consisting of an input layer (6 neurons), two hidden layers (containing 4 and 3 neurons respectively), and the output layer with one neuron. A non-linear activation function **leaky-relu** [$f(z) = \max(0, z) + 0.01 * \min(0, z)$] is used between the input and hidden layers to counter typical convergence problems found in small ANNs. We used the state of the art gradient descent benchmark optimizer Adam⁹⁹, as implemented in `tensorflow`¹⁰⁰ in the Keras API¹⁰¹.

C. Performance comparison

For the regression model, given an ML fit, we use two common statistical measures of error applied to the H_c predictions: (i) Mean Square Error (MSE):

$$\text{MSE} = \frac{1}{N} \sum_i^N (y_i - y_{\text{pred}_i})^2, \quad (9)$$

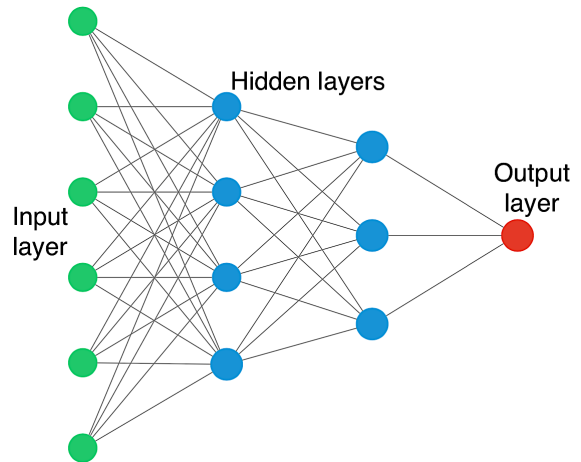


FIG. 2. Schematic diagram showing an artificial neural network (only a portion used in the calculations) with 6 neurons in the input layer, 4 and 3 neurons in the second and the third deep (hidden) layers, and a neuron for regression in the output layer. Two different ANN's were used in actual calculations, as discussed in the main text.

which is also used for training all ML models, and (ii) R-squared (R^2):

$$R^2 = 1 - \frac{\text{MSE}}{V(y)}, \quad (10)$$

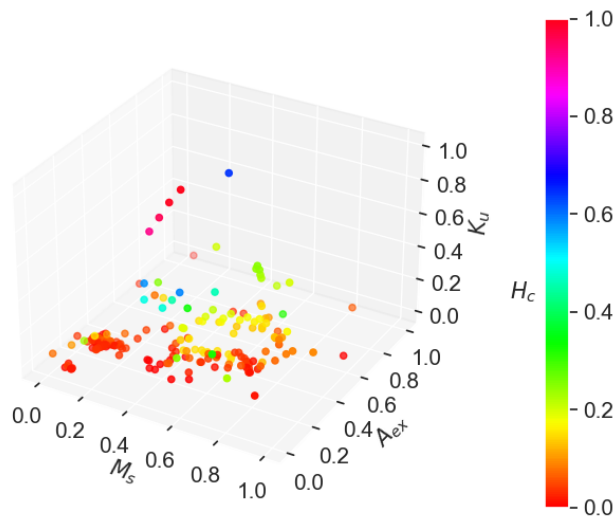


FIG. 3. The distribution of H_c as a function of M_s , A_{ex} , and K_u in experimental magnetic materials. The physical quantities are rendered as normalized and dimensionless. The color map shows the magnitude of H_c .

where $V(y)$ is the variance written as

$$V(y) = \langle (y_i - \langle y \rangle)^2 \rangle \quad (11)$$

with $\langle y \rangle$ as the mean of the predicted values. Equivalently, we may write $R^2 = 1 - \text{RSS}/\text{TSS}$, where RSS is the Residual Sum of Squares $\text{RSS} = \sum_i^N (y_i - y_{\text{pred}_i})^2$, and TSS is the Total Sum of Squares $\text{TSS} = \sum_i^N (y_i - \langle y \rangle)^2$. The loss function is usually written as a sum of the MSE and the first or second-order norms of the target function parameters. This provides convergence of the model, and penalizes overfitting for parameterized machine learning.

D. Results and discussion

1. Machine learning on experimental data

Here, we explore the experimental data and the relation between target and independent variables. Fig. 3 visualizes H_c as a function of K_u , M_s , and A_{ex} . The actual values of the variables differ by several orders of magnitude. They are scaled using the `sci-kit minmaxscalar` in which a dimensionless scaled feature variable x_{scaled} in the range $[0,1]$ is obtained using the following relation:

$$x_{\text{scaled}} = \frac{(x - x_{\text{min}})}{(x_{\text{max}} - x_{\text{min}})}, \quad (12)$$

where x_{min} and x_{max} are minimum and maximum values of the feature variable x . Fig. 3 shows an increase of H_c with K_u , a decrease with M_s , and very little variation with A_{ex} .

TABLE II. Comparison of R^2 and MSE metrics in different ML models on test data sets for experimental materials. The non-linear regression models show better values of R^2 and MSE than the linear models. The error is evaluated over the difference of the logarithm of the coercivity in T.

Model	R^2	MSE
Linear regression	0.62	0.64
Lasso	0.38	1.07
Ridge	0.63	0.64
Lasso-CV	0.61	0.68
Ridge-CV	0.63	0.66
Elasticnet	0.62	0.66
DT regressor	0.89	0.19
DT pruned	0.84	0.27
RF regressor	0.87	0.23
gradient boosting (GB) regressor	0.80	0.34
Tuned GB regressor	0.87	0.22
XGB regressor	0.87	0.23
Tuned XGB regressor	0.89	0.18
ANN (Adam)	0.64	0.62
light gradient boosted machine (LGBM)	0.70	0.60
Fine tuned ANN	0.85	0.25

In gradient-based algorithms, such as ANN, additive relationships are easier to model than multiplicative ones, so the independent and dependent variables are logarithmically scaled. Accordingly, the measures of model performance are given in terms of the logarithm of the H_c . As a result of this change, the absolute measure of R^2 is increased by ~ 0.01 for all gradient-based models.

Figure 4 shows a comparison of ML and experimental H_c for the test dataset. The XGB-tuned model shows better performance than ANN-Adam. Table II shows the performance of various ML models. The linear models show poor performance, with $R^2 \ll 1$. This demonstrates the complex non-linear relation between the dependent and independent variables. The non-linear models DT, XGB, and RF perform better, with R^2 values of 0.89, 0.87, and 0.87, respectively. These values still witness a decrease from the R^2 scores of more than 0.9 on the training dataset.

The ANN model has R^2 scores that are similar to other classical models (see Table II). The ANN architecture using (dense layers=64, activation function=leaky_relu, dense layers=32, activation function=leaky_relu, dense layers=16, activation function=leaky_relu, and output layer=1, and learning rate=0.007, epochs=1000, batch size=24) showed similar R^2 scores to RF. This weak performance for the ANN architecture is attributed to the smallness of the dataset size.

Feature importance. The model performance can be further validated from the dependence of H_c on the independent features. We compute the importance of RF features by utilizing the model-agnostic interpretive features of `scikit-learn` on the RF and XGB regression models¹⁰². The feature importance is computed by the

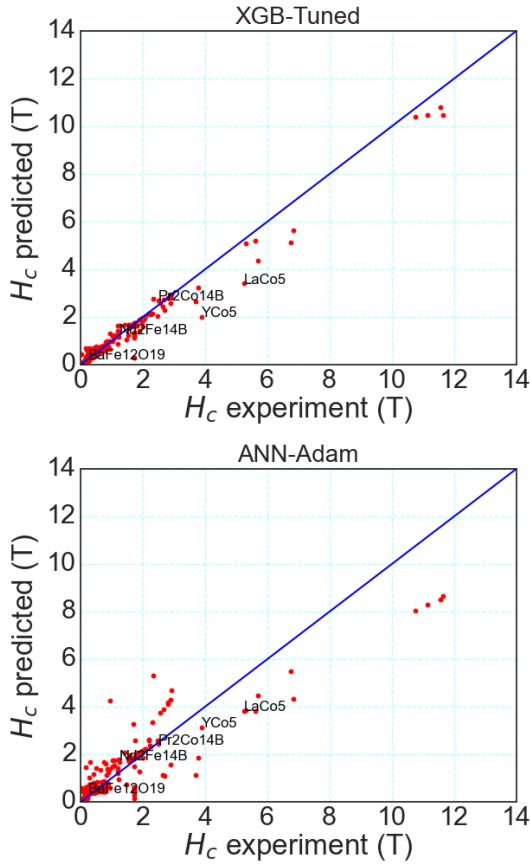


FIG. 4. ML predicted and experimental coercivities of magnetic materials obtained with tuned XGB (*top*) and ANN (*bottom*). Selected key materials are labeled in the figure. Non-linear regressors all yield similar results.

Gini index

$$\text{Gini index} = 1 - \sum_i p_i^2, \quad (13)$$

where p_i is the probability of class i in the data. Fig. 5 depicts the relative importance of the independent parameters for H_c , as computed by the XGB model. ML accurately identifies K_u as the leading contributing feature to H_c . More surprisingly, the effect of M_s is about four times smaller than that of K_u . The uneven distribution of magnetic materials (shown in Fig. 3), and a constant noise level, may explain the unequal weighting of K_u and M_s . Finally, we note that A_{ex} has a comparatively minimal effect on H_c .

2. Machine learning prediction from micromagnetic data

In order to explore the relation between H_c and the independent variables, we used 8770 micromagnetic simulation-generated data points as a training set. The correlation between variables is given by Pearson's cor-

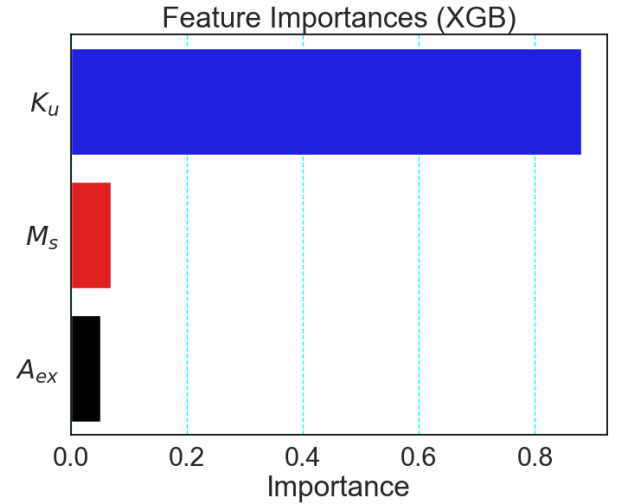


FIG. 5. Histogram of important features contributing to H_c in the XGB model. The K_u clearly leads, followed distantly by M_s and A_{ex} .

relation coefficient, which is defined as

$$r = \frac{\sum (X_1 - \langle X_1 \rangle)(X_2 - \langle X_2 \rangle)}{\sqrt{\sum (X_1 - \langle X_1 \rangle)^2 \sum (X_2 - \langle X_2 \rangle)^2}}, \quad (14)$$

where X_i and $\langle X_i \rangle$ denote the variable i and its average value. A positive (or negative) value of r indicates a positive (or negative) correlation between the two variables: the higher the r -value, the higher the correlation. Fig. 6 shows a correlation heatmap for the variables. The distribution for the 8770-data set is right-skewed, as shown in Fig. 7, with a peak around 0.2–0.4 T. It is similar to the distribution for the experimental materials (not shown here): most of the materials have values around the peak, and a few materials, such as 1:5 compositions, have larger values of 2–6 T. For better ML training, logarithmic transformation is appropriate for skewed data, which is employed in our model fits.

Significantly, the strongest (absolute) correlation is observed between H_c and K_u at 0.66, followed by M_s with a correlation of -0.62 , and then by A_{ex} at 0.2. This pattern suggests a high dependence of H_c on K_u . The negative correlation between H_c and M_s aligns with the theoretical relationship $H_c \propto M_s^{-1}$. Similarly, the correlation coefficient (r) between H_c and K_u or A_{ex} validates the proportionalities $H_c \propto K_u$ and $H_c \propto A_{ex}$. These findings are consistent with the trends observed in actual materials, as illustrated in Fig. 3.

Next, we discuss the model performance in micromagnetic simulation data, as given in Table III. Both linear and non-linear models perform well, as the R^2 score is above 0.9. This is expected in a linear regression model where multivariate analysis demonstrates very little multicollinearity in randomly generated independent variables. The multicollinearity can be measured with the variance inflation factor (VIF) $VIF_\alpha = (1 - R_\alpha^2)^{-1}$, where

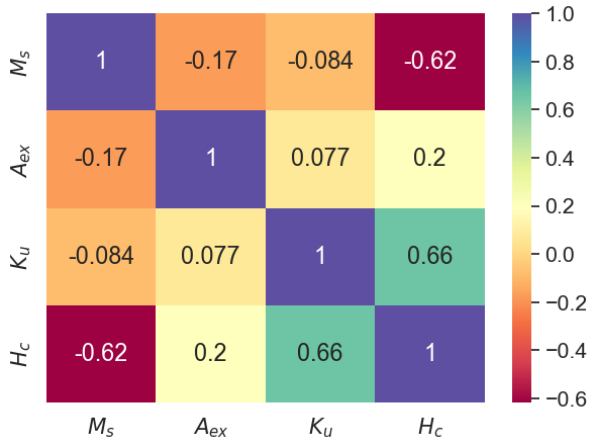


FIG. 6. Heat map showing the correlation between the H_c , A_{ex} , K_u , and H_c . The color palette corresponds to the correlations between the variables. H_c is strongly correlated with K_u , negatively correlated with M_s , and weakly correlated with A_{ex} . M_s shows a slightly negative correlation with K_u and A_{ex} . K_u shows a slightly positive correlation with A_{ex} .

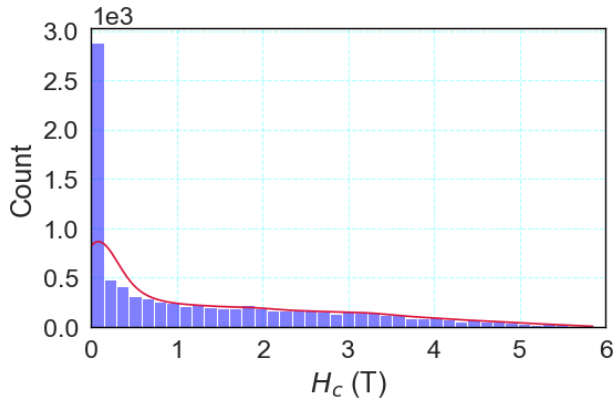


FIG. 7. Distribution of H_c in the training set of 8770 data points. The y -axis is scaled by 10^3 . The data points are right-skewed.

R_α^2 is the R^2 [Eq. (10)] value of H_c considered as a function of variable α . The computed VIF factors are 1.53 for M_s , 4.36 for A_{ex} , and 1.53 for K_u .

More advanced decision tree regressors improve the performance. XGB, as the most accurate model, was used as a benchmark, with the hyperparameters given in Appendix A for H_c prediction from experimental data. The deviance in the MSE of the training and testing data sets is shown in Fig. 14. ANNs exhibit performance similar to other non-linear regressors. The ANN is as follows: (dense layers=64, activation function=leaky_relu, dense layers=32, activation function=leaky_relu, dense layers=16, activation function=leaky_relu, and output layer=1, and learning rate=0.007, epochs=1000, batch size=56). To obtain a deeper insight into ML predictability, the experimental, scaled-micromagnetic, and ML-

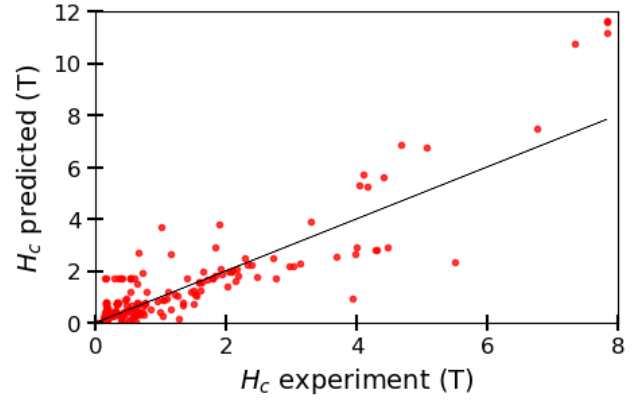


FIG. 8. Scatter plot showing the comparison of experimental and ML-mumax³ (ML-micromagnetics data) predicted H_c for experimental materials.

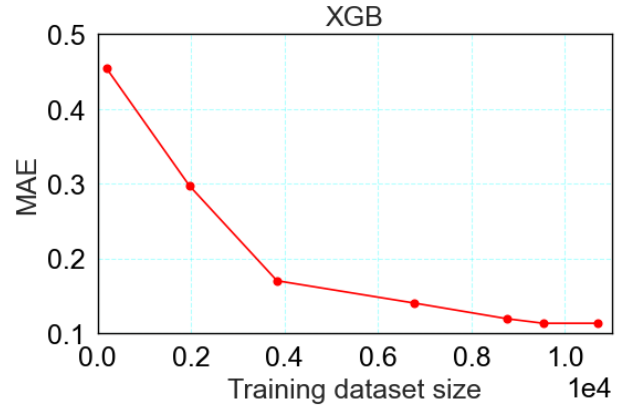


FIG. 9. MAE convergence for H_c with respect to training data set size in XGB model. The x -axis is in the scale of 10^4 .

predicted H_c values are compared with only the known important rare-earth-based materials in Table IV. In general, ML-predicted values are smaller than the micromagnetically computed values. For 2:14:1 rare-earth magnets, ML improves the results. For 1:5 rare-earth magnets, it slightly underestimates the experiment. The full comparison of experimental and ML predicted data is given in Fig. 8

Additionally, XGB was trained with different fractions of the dataset, from 200 to 12000, by computing the mean absolute error (MAE) error metric:

$$\text{MAE} = \sum_i^N \frac{|y_i - y_{pred_i}|}{N} \quad (15)$$

Fig. 9 shows the convergence of the MAE (obtained with the XGB model) plotted against the training data set size, indicating that the model performs well for datasets with more than 6000 points.

Next, we discuss the loss function RMSE to examine the model performance. We computed the root mean

TABLE III. mumax³ data on hypothetical materials: Comparison of R^2 and MSE of H_c for different ML models. All the errors are evaluated over the ln of the H_c in T. The fine-tuned model hyperparameters are given in Appendix A.

Model	R^2	MSE
Linear regression	0.95	0.22
Lasso	0.54	2.13
Ridge	0.95	0.22
Lasso-cv	0.95	0.25
Ridge-cv	0.95	0.22
Elasticnet	0.94	0.26
DT regressor	0.97	0.13
DT pruned	0.97	0.15
RF regressor	0.98	0.08
GB regressor	0.98	0.09
Tuned GB regressor	0.98	0.08
XGB regressor	0.98	0.98
Tuned XGB regressor	0.98	0.08
ANN	0.98	0.09

square error (RMSE) as

$$\text{RMSE} = \sqrt{\frac{1}{N} \sum_{i=1}^N (y_i - \hat{y}_i)^2}, \quad (16)$$

where y and \hat{y} refer to the experimental and ML/mumax³ predicted values. Remarkably, the RMSE and MAE between experimental and ML (tuned XGB) predicted values are smaller than the RMSE between experimental and the scaled-mumax³, indicating that ML helps to correct the mumax³ predictions. It also shows how the H_c is correlated with other features. Moreover, ML is an order of magnitude computationally faster than mumax³, and we can use the trained model for predicting H_c in new materials without any mumax³ calculations.

IV. ML APPLICATION WITH DFT

Our computational H_c predictions involve two steps: DFT for Ce-doped Nd₂Fe₁₄B, and then ML trained on micromagnetically generated databases with input parameters from the DFT computations.

A. DFT methods and crystal structure

We used the Vienna simulation package (VASP)^{103,104} with the projector augmented wave (PAW) formalism in the generalized gradient approximation (GGA) of Perdew-Burke-Ernzerhof (PBE) semi-local exchange-correlation functionals^{105,106} including onsite electron-electron correlation Dudarev-Hubbard¹⁰⁷ $U_{\text{eff}} = U - J$ for the $4f$ states of Nd, and spin-orbit interaction. The kinetic energy cut-off is 520 eV for the plane wave expansion, with a $4 \times 4 \times 2$ \mathbf{k} -mesh for the Brillouin zone

TABLE IV. H_c (in T) comparisons among experiment, ML prediction, and scaled mumax³ for different permanent magnetic materials. The ML (tuned XGB and ANN) predictions are obtained by training the hypothetical materials using the random independent variables M_s , A_{ex} , and K_u , and the mumax³ computed H_c . RMSE and MAE quantify the discrepancy between the experimental ML and the mumax³ scaled cH_c .

Material	$H_c(\text{exp})$	$H_c(\text{XGB})$	$H_c(\text{ANN})$	cH_c
La ₂ Fe ₁₄ B	0.52	0.52	0.48	0.53
Ce ₂ Fe ₁₄ B	0.54	0.84	0.73	0.79
Pr ₂ Fe ₁₄ B	1.54	1.59	1.54	1.62
Nd ₂ Fe ₁₄ B	1.24	1.50	1.45	1.56
Gd ₂ Fe ₁₄ B	0.23	0.56	0.52	0.60
Tb ₂ Fe ₁₄ B	2.93	4.00	5.65	5.41
Dy ₂ Fe ₁₄ B	1.70	2.76	3.80	3.70
Ho ₂ Fe ₁₄ B	0.75	1.50	1.76	1.82
Lu ₂ Fe ₁₄ B	0.29	0.59	0.52	0.58
Y ₂ Fe ₁₄ B	0.19	0.57	0.48	0.54
Th ₂ Fe ₁₄ B	0.17	0.56	0.48	0.53
La ₂ Co ₁₄ B	0.34	0.65	0.68	0.77
Pr ₂ Co ₁₄ B	2.50	2.28	2.24	2.36
Nd ₂ Co ₁₄ B	3.69	1.00	0.90	1.06
Gd ₂ Co ₁₄ B	0.30	0.67	2.79	2.37
Y ₂ Co ₁₄ B	0.34	0.62	0.61	0.71
NdLaCeFe ₁₄ B	0.65	1.33	1.25	1.39
LaCeYFe ₁₄ B	0.41	0.99	1.26	1.39
NdPrFe ₁₄ B	0.80	1.33	1.27	1.39
Sm ₂ Co ₁₇	1.25	1.60	1.53	1.62
Sm ₂ Fe ₁₇ N ₃	2.30	2.46	3.13	2.95
SmCo ₅	7.50	6.76	6.66	9.70
YCo ₅	3.90	2.63	2.68	3.33
LaCo ₅	5.25	4.18	4.14	4.22
CeCo ₅	5.70	4.10	5.10	5.17
PrCo ₅	5.32	4.05	3.81	4.02
NdCo ₅	0.15	0.12	0.10	0.12
RMSE		0.90	1.10	1.10
MAE		0.68	0.78	0.80

integration. The experimental structure was used in calculations to avoid overestimating bond lengths lengths and lattice constants in the PBE.

The crystal structure of Nd₂Fe₁₄B is tetragonal with 68 atoms (4 formula units), having space group $P42/mnm$ (136) and lattice constants $a = b = 8.80$ and $c = 12.20$ Å, taking $\alpha = \beta = \gamma = 90^\circ$ at a temperature $T = 285$ K^{20,108}, with experimental parameters for full Ce-doped Nd₂Fe₁₄B¹⁰⁹. The crystal structure of the 2:14:1 neo-magnet is shown in Fig. 10, which consists of rare-earth Nd in the 2 inequivalent sites $4f$ and $4g$, transition element Fe in the 6 inequivalent sites at $16k$, $16k$, $8j$, $8j$, $4e$, and $4c$, and finally B at the $4f$ sites. Fully self-consistent spin-orbit calculations, i.e., PBE+ U +spin-orbit coupling (SOC), were performed to obtain the magnetic anisotropy energy along with the spin and orbital magnetic moments.

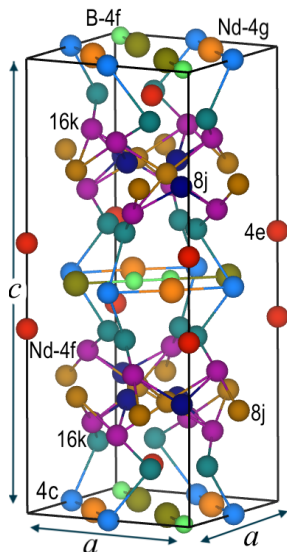


FIG. 10. Crystal structure of $\text{Nd}_2\text{Fe}_{14}\text{B}$ occupied by Nd at two non-equivalent sites $4f$ and $4g$, Fe at six inequivalent sites $16k$, $16k$, $8j$, $8j$, $4c$, and $4e$ (labeled by Wyckoff positions), and B at the $4f$ site.

B. Magnetic properties

Here we discuss the PBE+ U +SOC results with $\text{Nd}_2\text{Fe}_{14}\text{B}$, using ML for H_c prediction. Hubbard U -correction is necessary for highly correlated $3d$ and $4f$ elements^{110–113} to accurately predict K_u . We performed test calculations for various values of U from 4–7 eV for Nd $4f$ orbitals. Table V shows the spin and orbital magnetic moments of Nd, Fe, and B at different crystallographic sites for different values of U_{eff} . The non-magnetic B atom carries negligible magnetic moments. Nd exhibits an Nd^{3+} state with spin magnetic moment (μ_s) of ~ -3.3 and strongly quenched orbital moment (μ_l) of $\sim 1.5 \mu_B$ due to the crystalline electric field. The spin and orbital moments have opposite signs, consistent with Hund’s rule for a less than half-filled $4f$ shell. The net magnetic moment is robust, and does not vary significantly with U .

Table VI lists K_u , M_s , T_C , and their comparison with experimental values. K_u is positively correlated with U . The experimental K_u is 4.5 MJ/m^3 ¹¹⁴ at 300 K, which corresponds to the computed value for $U \sim 4 \text{ eV}$. T_C is computed with the static Green’s function (GF) as implemented in ASA in the local density approximation (LDA)¹¹⁵ for the exchange-correlation functional in the linearized muffin-tin orbital (LMTO) program^{116,117}. The pair exchange interaction $J_{RR'}$ between magnetic R and R' ions is computed using the Lichtenstein formula¹¹⁸, from which T_C is estimated. The calculated Weiss mean-field theory¹¹⁹ value of 718.1 K is larger than the experimental value, which is expected in the mean-field approximation (MFA). According to a

spin-wave theory by Tyablikov¹²⁰, the random-phase approximation (RPA) corrects the value, bringing it down to 539.1 K. The experimental value lies within the MFA and RPA limits.

Next, we discuss the site-resolved spin-orbit anisotropy energy which is computed as $E_{\text{anis}} = E_{100} - E_{001}$ ¹¹¹, where E_{100} and E_{001} are PBE+ U +SOC-computed atomic site energies for spin-quantization along the $[100]$ and $[001]$ directions. Generally, $4f$ -elements contribute to K_u , and $3d$ -elements contribute to the magnetic moments in rare-earth-based magnets. The spin moments of the rare-earth ion are anti-parallel to the spin moment of the $3d$ ion, which is also the case for neo-magnets. The site contribution of the Nd-element to crystalline anisotropy energy is given in Table VII. In our PBE+ U +SOC calculations, we did not impose symmetry, which means that all the atoms are inequivalent under the P_1 crystal symmetry. All eight Nd atoms split into eight different sites. The individual on-site energies differ significantly for the atoms of the same crystallographic site. Interestingly, at least one Nd (Nd_1) at $4f$ has a negative contribution to crystalline anisotropy energy, as given in Table VII. Theoretically, it can be inferred that Nd has a tendency to be planar at the $4f$ site, differing from the $4g$ site, which is strictly uniaxial along the crystalline c direction. These results are consistent with experiment¹²¹.

Table VIII shows the computed values of the magnetic moments and magnetic anisotropy in the Ce-substituted neo-magnet at Nd- $4f$ sites. The Ce-atom carries a small spin magnetic moment $\sim 1\mu_B$ compared to the Nd $\sim 3\mu_B$ moment. Moreover, the orbital moment does not entirely cancel the spin moment in Nd, unlike in Ce, where the net spin + orbital moment vanishes. Therefore, there is an increase in the net magnetic moment with Ce. On the other hand, magnetic anisotropy is reduced because the Ce-site contribution is much smaller than that of Nd. The calculated value of K_u slightly underestimates the experiment (see Table I), which is reasonable, given the choice of the U -values used for the Ce and Nd $4f$ states. We used $U_{\text{eff}} = 2 \text{ eV}$ for Ce and 4 eV for Nd in the calculations.

C. ML coercivity prediction

Central to this paper is the hypothesis that macroscopic measures of H_c are not well predicted by theory, while the microscopic magnetic parameters M_s , K_u , and A_{ex} are. However, knowledge of the microscopic parameters is sufficient to produce realistic estimates of H_c by accumulating a database and modeling it with ML. Furthermore, once an ML prediction is made, information about the material grain structure may be reverse-engineered with micromagnetic modeling. Although material fabrication variations have a significant impact on H_c , this section demonstrates the surprising effectiveness of the methodology as applied to $\text{Nd}_2\text{Fe}_{14}\text{B}$, with and

TABLE V. Spin and orbital magnetic moments (μ_s and μ_l) of individual atoms in different Wyckoff positions, and total magnetic spin and orbital magnetic moments (μ_{st} and μ_{lt}) per unit cell (in μ_B), in $\text{Nd}_2\text{Fe}_{14}\text{B}$ computed using the PBE+ U +SOC method with various values of U for the Nd ($4f$) electronic states. There are two $16k$ and $8j$ sites, therefore, the pairs are given. The μ_l of the pair at $8j$ -sites do not differ, and only one value is given to represent both atoms.

atom→	Nd($4f$)		Nd($4g$)		Fe($16k$)		Fe($8j$)		Fe($4e$)		Fe($4c$)		B($4g$)		total	
	μ_s	μ_l	μ_s	μ_l	μ_s	μ_l	μ_s	μ_l	μ_s	μ_l	μ_s	μ_l	μ_s	μ_l	μ_{st}	μ_{lt}
4 eV	-3.26	1.52	-3.28	1.53	2.27,2.36	0.043,0.049	2.29,2.71	0.044	2.03	0.045	2.48	0.054	-0.17	0.00	105.24	14.75
5 eV	-3.26	1.52	-3.28	1.53	2.27,2.36	0.042,0.048	2.29,2.70	0.044	2.03	0.045	2.47	0.052	-0.17	0.00	105.25	14.75
7 eV	-3.27	1.52	-3.28	1.53	2.27,2.36	0.042,0.048	2.29,2.71	0.042	2.03	0.044	2.48	0.049	-0.17	0.00	105.25	14.68

TABLE VI. Calculated K_u in MJ/m^3 , M_s in $\mu_B/\text{f.u.}$ using PBE+ U +SOC, T_C in Kelvin (K) using Green's function-ASA (LDA), and comparison with available experiment.

U	K_u	M_s	$M_s(\text{Expt}^{20})$	T_C	$T_C(\text{Expt}^{20})$
4 eV	6.16	29.98	37.7 ^a , 32.5 ^b	718.1 ^c , 539.1 ^d	585
5 eV	8.56	30.00
7 eV	11.58	30.01

^a at low temperature, (4 K)

^b at high temperature (295 K)

^c Mean Field Approximation (MFA)

^d Random Phase Approximation (RPA)

TABLE VII. Site resolved spin-orbit anisotropy energy (E_{anis}) in meV of the Nd contribution to magneto-crystalline anisotropy energy. In PBE+ U +SOC calculations, the crystalline symmetry lowers to the P_1 point group implying that the atoms (including the Nd) split into eight sites. The negative value for Nd at the $4f$ site indicates it produces a planar contribution to the crystalline anisotropy energy, consistent with experiment¹²¹.

Atom	Wyckoff-position	E_{anis}
Nd ₁	$4f$	1.3780
Nd ₂	$4f$	-1.1914
Nd ₃	$4f$	0.5336
Nd ₄	$4f$	6.2204
Nd ₅	$4g$	0.4865
Nd ₆	$4g$	3.8064
Nd ₇	$4g$	6.2094
Nd ₈	$4g$	3.0622

without Ce doping.

The *ab initio*-calculated values were fed to the tuned XGB ML model to produce the output predictions. Additionally, micromagnetic simulation was used to determine a hysteresis loop. The results are depicted in Table IX. As can be seen, the reduction trend of H_c

TABLE VIII. Total spin, orbital, and spin + orbital magnetic moments μ_s , μ_l , and $\mu_s + \mu_l$ in μ_B/cell , K_u in MJ/m^3 , and M_s in MA/m of $\text{Ce}_2\text{Fe}_{14}\text{B}$ and $\text{Nd}_2\text{Fe}_{14}\text{B}$.

Properties	$\text{Nd}_2\text{Fe}_{14}\text{B}$	$\text{Ce}_2\text{Fe}_{14}\text{B}$
μ_s	105.24	120.73
μ_l	14.75	4.55
$\mu_s + \mu_l$	119.99	125.28
K_u	6.16	1.21
M_s	1.31	1.24

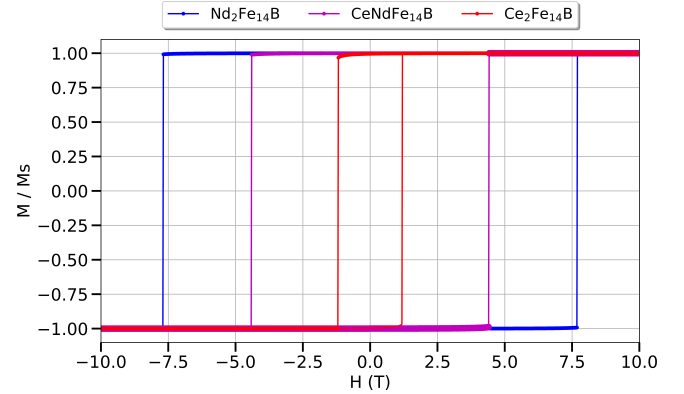


FIG. 11. Hysteresis curve for $\text{Nd}_{2-x}\text{Ce}_x\text{Fe}_{14}\text{B}$ ($x = 0, 1.0, 2.0$) calculated from micromagnetic simulation. Ce leads to the reduction in the coercivity. M/M_s is the reduced magnetization.

with Ce is similar to that found experimentally¹²². Further, we computed the ML [trained with experiment (ML-Exp) and scaled micromagnetic data (ML-mumax³) separately] and scaled micromagnetic simulated H_c for SmCo_5 , YCo_5 , CeZrFe_{11} , $\text{CeZrFe}_{11}\text{N}$, CeTiFe_{11} , and $\text{CeTiFe}_{11}\text{N}$ using DFT intrinsic parameters as given in Table IX. The ML-exp predicts inconsistent H_c due to the small data size training, as evident from model performance metrics in Tab II. The ML-mumax³ trained on big data sets produces more sensible H_c than scaled-

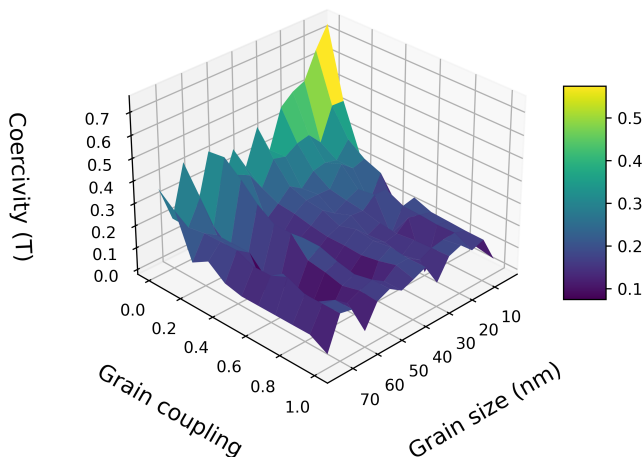


FIG. 12. Coercivities for different inter-grain couplings for $\text{Nd}_2\text{Fe}_{14}\text{B}$, measured as a function of the ratio of inter-grain exchange stiffness to intra-grain exchange stiffness and different grain sizes. As the material is complex, a cuboid of $128 \times 128 \times 128 \text{ nm}^3$ was generated for each grain size, resulting in some random undulations according to grain initialization. The plot displays a decreasing coercivity with increasing grain size as observed in experiment¹²².

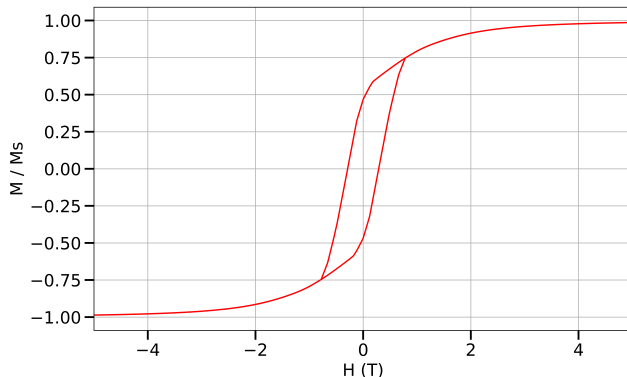


FIG. 13. Hysteresis curve for $\text{Ce}_2\text{Fe}_{14}\text{B}$ calculated naively with micromagnetic simulation with grain size set to 30nm and intergrain stiffness to intragrain stiffness set at 0.58 to recreate the ML H_c prediction.

micromagnetics and ML-exp. For SmCo_5 , micromagnetic simulation yielded a factor of three larger H_c than the ML-mumax³ model and experiments. For YCo_5 , the ML-mumax³ model produced slightly lower H_c than the experiment, attributed to the DFT underestimate of K_1 . Overall the ML-mumax³ model consistently tends to correct the micromagnetically predicted H_c towards experiments for known materials (see Table I).

If the fabricated material is grown as a crystal with well-defined grains, it is possible to reverse-engineer the structure. The dependence of H_c on micromagnetic pa-

TABLE IX. Comparison of ML predicted and scaled-micromagnetic (cH_c) H_c in T for materials with calculated DFT parameters. ML-exp/ML-mumax³ represent to predictions made by training experimental/scaled-micromagnetic data.

Material	ML-Exp	ML-mumax ³	cH_c
$\text{Nd}_2\text{Fe}_{14}\text{B}$	3.92	2.39	2.35
$\text{CeNdFe}_{14}\text{B}$	0.88	1.27	1.29
$\text{Ce}_2\text{Fe}_{14}\text{B}$	0.39	0.40	0.36
SmCo_5	8.87	5.88	18.12
YCo_5	1.45	1.51	1.60
CeZrFe_{11}	6.25	4.93	5.99
$\text{CeZrFe}_{11}\text{N}$	1.51	2.15	2.59
CeTiFe_{11}	1.50	2.09	2.70
$\text{CeTiFe}_{11}\text{N}$	1.51	1.92	2.45

rameters viz, grain sizes and inter-grain coupling is visualized in Fig. 12 in $128 \times 128 \times 128 \text{ nm}^3$ magnetic cell. Here the grain coupling refers to a reduction factor to the stiffness exchange coupling A_{ex} . We note that we did not find much difference in the results with the use of $64 \times 64 \times 64$ and $128 \times 128 \times 128 \text{ nm}^3$ simulation cells. Although non-linear, we find a similar trend of H_c with inter-grain exchange coupling and grain sizes. For a fixed value of grain size, qualitatively, H_c decreases with inter-grain exchange coupling, while it is the opposite with grain size. That inter-grain exchange coupling may not be uniform in actual material due to the void or imperfection between the grains, which affects the perfect spin alignment resulting in M_s . A larger inter-grain exchange coupling further reduces K_1 and H_c . With an increase in grain size, H_c experiences a decrease, similar to that reported in the Dy-substituted neo-magnet¹²³.

Various combinations of grain size and inter-grain exchange coupling reproduce the actual coercivity. For instance, with grain size $\sim 30 \text{ nm}$, and a 0.58 ratio for inter-grain to intra-grain A_{ex} reproduces the realistic H_c of 0.40 T, as demonstrated in Fig. 13. Strictly speaking, a larger inter-grain coupling tends to reduce the H_c , regardless of grain size. This suggest that we can explore the other magnetic parameters A_{ex} and grain size by using ML-predicted results employing micromagnetic simulations, which demonstrates the fundamental usefulness of ML, not just as a black box, but also as a pre-processing input to a micromagnetic model to reverse-engineer the micromagnetic structure.

V. CONCLUSION

Experimental dataset input and ML modeling coupled with DFT predicts H_c with far greater accuracy and

speed than was previously possible using micromagnetic modeling. This technique provides a robust computational foundation for predicting novel permanent magnet materials and optimizing their properties. Using micromagnetic simulation, we first studied magnetization as a function of the applied magnetic field for real and hypothetical magnetic materials, mainly focusing on 1:5 and 2:14:1 rare-earth-based permanent magnets such as $\text{Nd}_2\text{Fe}_{14}\text{B}$. Calculations of H_c based on the hysteresis loop overestimate by a factor of ~ 5 ; the Brown Paradox. The paradox is side-stepped by the judicious use of ML, obtaining a more accurate prediction of the target variable by learning its dependence on the input features. We find that H_c is directly proportional to K_u , inversely proportional to M_s , and weakly correlated with A_{ex} .

We apply the ML modeling to $\text{Nd}_2\text{Fe}_{14}\text{B}$ by first computing its independent variables with DFT calculations. These calculations show that the Nd $4g$ -sites mainly contribute to the uniaxial magneto-crystalline anisotropy. They also yield a value for the T_C , which agrees with the experiment. The DFT predictions suggest the possibility of tuning rare-earth magnetic properties by substituting non-critical elements at specific sites. For instance, Ce-doping at $4f$ sites shows only a slight reduction in H_c , consistent with the ML prediction. Finally, we engineer the grain boundary size and inter-exchange coupling with the aid of ML-predicted H_c , which indicates that the reduction in inter-grain exchange coupling reduces H_c . On the other hand, reducing the grain size increases H_c qualitatively.

ACKNOWLEDGMENTS

This work is supported by the Critical Materials Innovation Hub, an Energy Innovation Hub funded by the US Department of Energy, Office of Energy Efficiency and Renewable Energy, Advanced Materials and Manufacturing Technologies Office. The Ames National Laboratory is operated for the U.S. Department of Energy by Iowa State University of Science and Technology under Contract No. DE-AC02-07CH11358. GNN acknowledges support from the U.S. Department of Energy, Office of Science, Office of Workforce Development for Teachers and Scientists, Office of Science Graduate Student Research (SCGSR) program. The SCGSR program is administered by the Oak Ridge Institute for Science and Education for the DOE under contract number DE-SC0014664.

Appendix A: ML model and hyperparameter tuning

In this appendix we provide information about the hyperparameters used in the fine tuning of the ML models. With the experimental data, we used the hyperparameters given in Table X for tuned XGB model training.

TABLE X. Hyperparameters used for XGB model training of experimental magnetic materials.

n_estimators=500
min_weight_fraction_leaf=0
max_depth=5
learning_rate=0.006

In mumax³ data training we use the hyperparameters given in Table XI.

The hyperparameter used in the fine-tuned GBR model training is shown in Fig. 14. The deviance (MSE) converges well in both the test and training datasets after 600 boosting iterations, confirming a very good model performance.

Appendix B: DFT parameters for 1 : 5 and 1 : 12 intermetallics

Table XII provides the DFT computed parameters for 1 : 5 and 1 : 12 intermetallic compounds.

TABLE XI. Fine-tuned hyperparameters for different ML models used in the training of micromagnetic simulated data.

Model	Hyperparameters
Tuned RF	n_estimators=1200, max_depth=5, random_state=1, min_samples_leaf=3, bootstrap=True, max_features='auto'
Tuned XGB	n_estimators=1200, max_depth= 5, min_weight_fraction_leaf=0, learning_rate=0.007
Tuned XGB	n_estimators= 1200, max_depth= 5, min_child_weight=0, learning_rate=0.007, random_state=42

[1] J. F. Trevor Hastie, Robert Tibshirani, *The Elements of Statistical Learning*, second edition ed., Springer Series in Statistics No. 2 (Springer New York, NY) pp. XXII,

745.

[2] M. J. Crowder, *Statistical Analysis of Reliability Data*, 1st ed. (CHAPMAN & HALL/CRC, 1991).

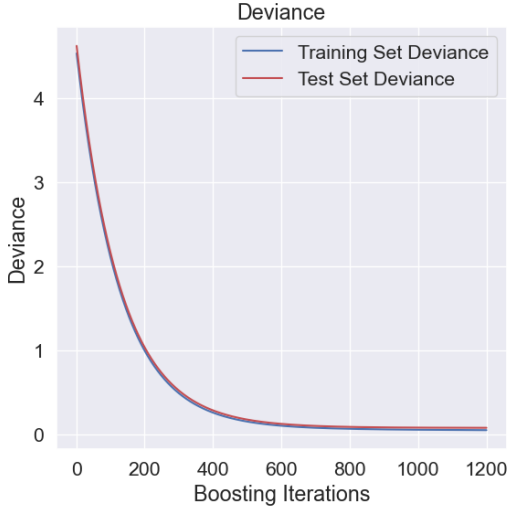


FIG. 14. Deviance as a function of boosting iterations for the micromagnetic simulated dataset with XGB model. Deviance is MSE between the actual and predicted data set computed in each iteration. Both the training and test data set converge well after 600 boosting iterations.

TABLE XII. DFT computed intrinsic magnetic parameters for 1 : 12 compositions taken from our previous work¹¹³ except for 1 : 5 type materials as referred in Table. A_{ex} is kept fixed for all materials.

Material	M_s (A/m)	A_{ex} (pJ/m)	K_u (MJ/m ³)
SmCo ₅ ¹²⁴	1069768.213	7	40.27
YCo ₅ ¹²⁵	770449.2281	7	2.65
CeZrFe ₁₁	597220.2602	7	7.36
CeZrFe ₁₁ N	632804.6376	7	3.42
CeTiFe ₁₁	587261.7154	7	3.29
CeTiFe ₁₁ N	625792.1247	7	3.20

[3] W. F. Brown, Virtues and weaknesses of the domain concept, *Rev. Mod. Phys.* **17**, 15 (1945).
 [4] A. Aharoni, Theoretical search for domain nucleation, *Rev. Mod. Phys.* **34**, 227 (1962).
 [5] U. Hartmann, Origin of Brown's coercive paradox in perfect ferromagnetic crystals, *Phys. Rev. B* **36**, 2331 (1987).
 [6] T. Xie and J. C. Grossman, Crystal graph convolutional neural networks for an accurate and interpretable prediction of material properties, *Phys. Rev. Lett.* **120**, 145301 (2018).
 [7] F. A. Faber, A. Lindmaa, O. A. von Lilienfeld, and R. Armiento, Machine learning energies of 2 million elpasolite (ABC₂D₆) crystals, *Phys. Rev. Lett.* **117**, 135502 (2016).
 [8] D. Xue, P. V. Balachandran, J. Hogden, J. Theiler, D. Xue, and T. Lookman, Accelerated search for materials with targeted properties by adaptive design, *Nat. Comm.* **7**, 11241 (2016).

[9] A. Seko, A. Togo, H. Hayashi, K. Tsuda, L. Chaput, and I. Tanaka, Prediction of low-thermal-conductivity compounds with first-principles anharmonic lattice-dynamics calculations and bayesian optimization, *Phys. Rev. Lett.* **115**, 205901 (2015).
 [10] J. J. Hopfield, Neural networks and physical systems with emergent collective computational abilities., *Proc. Natl. Acad. Sci.* **79**, 2554 (1982), <https://www.pnas.org/doi/pdf/10.1073/pnas.79.8.2554>.
 [11] J. Hertz, A. Krogh, and R. G. Palmer, *Introduction to the Theory of Neural Computation*, 1st ed. (CRC Press, 1991).
 [12] M. Freaun, The upstart algorithm: a method for constructing and training feedforward neural networks, *Neur. Comp.* **2**, 198 (1990).
 [13] See supplemental material at supplementary, which includes refs. [20,27–81], for additional information about the experimental databases.
 [14] Q. Liu and Y. Wu, Supervised learning, in *Encyclopedia of the Sciences of Learning*, edited by N. M. Seel (Springer US, Boston, MA, 2012) pp. 3243–3245.
 [15] J. Schmidhuber, Deep learning in neural networks: An overview, *Neur. Netw.* **61**, 85 (2015).
 [16] T. K. Ho, Random decision forests, in *Proceedings of 3rd international conference on document analysis and recognition*, Vol. 1 (IEEE, 1995) pp. 278–282.
 [17] T. Gilbert, A phenomenological theory of damping in ferromagnetic materials, *IEEE Transactions on Magnetics* **40**, 3443 (2004).
 [18] W. F. Brown, *Micromagnetics* (Interscience Publishers New York, New York, 1963).
 [19] H. Kronmüller, General micromagnetic theory and applications, *Mater. Sci. Technol.* , 1 (2006).
 [20] J. F. Herbst, R₂Fe₁₄B materials: Intrinsic properties and technological aspects, *Rev. Mod. Phys.* **63**, 819 (1991).
 [21] A. Aharoni, *Introduction to the Theory of Ferromagnetism*, Vol. 109 (Clarendon Press, 2000).
 [22] C. Laplane, E. Z. Cruzeiro, F. Fröwis, P. Goldner, and M. Afzelius, High-precision measurement of the dzyaloshinsky-moriya interaction between two rare-earth ions in a solid, *Phys. Rev. Lett.* **117**, 037203 (2016).
 [23] C. Bhandari and D. Paudyal, Giant magnetic and optical anisotropy in cerium-substituted m-type strontium hexaferrite driven by 4 f electrons, *Phys. Rev. Appl.* **20**, 024016 (2023).
 [24] A. Vansteenkiste, J. Leliaert, M. Dvornik, M. Helsen, F. Garcia-Sanchez, and B. Van Waeyenberge, The design and verification of Mumax3, *AIP Adv.* **4**, 107133 (2014).
 [25] J. Leliaert, B. Van de Wiele, A. Vansteenkiste, L. Laurson, G. Durin, L. Dupré, and B. Van Waeyenberge, Current-driven domain wall mobility in polycrystalline permalloy nanowires: A numerical study, *J. Appl. Phys.* **115**, 233903 (2014).
 [26] L. Exl, S. Bance, F. Reichel, T. Schrefl, H. Peter Stimming, and N. J. Mauser, LaBonte's method revisited: An effective steepest descent method for micromagnetic energy minimization, *J. Appl. Phys.* **115**, 17D118 (2014).
 [27] N. Imamura and S. Chikazumi, Determination of exchange stiffness constant using high speed switching of fe-ni magnetic thin films, *J. Phys. Soc. Jpn.* **25**, 125

- (1968).
- [28] R. A. Ristau, K. Barmak, L. H. Lewis, K. R. Coffey, and J. K. Howard, On the relationship of high coercivity and L1 ordered phase in CoPt and FePt thin films, *J. Appl. Phys.* **86**, 4527 (1999).
- [29] B. C. Sales, B. Saporov, M. A. McGuire, D. J. Singh, and D. S. Parker, Ferromagnetism of Fe₃Sn and alloys, *Sci. Rep.* **4**, 7024 (2014).
- [30] H. Jaballah, W. Bouzidi, R. Fersi, N. Mliki, and L. Besais, Structural, magnetic and magnetocaloric properties of (Pr,Sm)₂Fe₁₇ compound at room temperature, *J. Phys. Chem. Solids* **161**, 110438 (2022).
- [31] Y. Iwama, M. Takeuchi, and M. Iwata, New determination of magnetic anisotropy constants of alnico magnet alloys, *J. Phys. Colloques* **32**, C1 (1971).
- [32] Y. Liu, J. Song, G. Liu, J. Chen, C. Wang, H. Wang, J. Wang, and X. Zhang, High strength and low coercivity of cobalt with three-dimensional nanoscale stacking faults, *Nano Lett.* **21**, 6480 (2021), pMID: 34324350.
- [33] H. Sato, T. Yoshioka, H. Tsuchiura, Y. Mizuno, K. Koike, K. Takahashi, and H. Kato, Rare-earth moment reduction and local magnetic anisotropy in Pr₂Fe₁₄B and Tm₂Fe₁₄B, *J. Magn. Magn. Mater.* **545**, 168684 (2022).
- [34] N. Yu, M. Zhu, L. Song, Y. Fang, K. Song, Q. Wang, and W. Li, Coercivity temperature dependence of Sm₂Co₁₇-type sintered magnets with different cell and cell boundary microchemistry, *J. Magn. Magn. Mater.* **452**, 272 (2018).
- [35] T. Kikuchi, T. Nakamura, T. Yamasaki, M. Nakanishi, T. Fujii, J. Takada, and Y. Ikeda, Magnetic properties of La-Co substituted M-type strontium hexaferrites prepared by polymerizable complex method, *J. Magn. Magn. Mater.* **322**, 2381 (2010).
- [36] K. M. U. Rehman, M. Riaz, X. Liu, M. W. Khan, Y. Yang, K. M. Batoo, S. F. Adil, and M. Khan, Magnetic properties of Ce doped m-type strontium hexaferrites synthesized by ceramic route, *J. Magn. Magn. Mater.* **474**, 83 (2019).
- [37] P. Wang, X. Wang, L. Qiao, J. Zhang, G. Wang, B. Duan, T. Wang, and F. Li, High-frequency magnetic properties and microwave absorption performance of oxidized Pr₂Co₁₇ flakes/epoxy composite in x-band, *J. Magn. Magn. Mater.* **468**, 193 (2018).
- [38] J. Zhang, H. Gao, Y. Yan, X. Bai, F. Su, W. Wang, and X. Du, Morphology and magnetic properties of CeCo₅ submicron flakes prepared by surfactant-assisted high-energy ball milling, *J. Magn. Magn. Mater.* **324**, 3272 (2012).
- [39] A. Gabay, X. Hu, and G. Hadjipanayis, Preparation of YCo₅, PrCo₅ and SmCo₅ anisotropic high-coercivity powders via mechanochemistry, *J. Magn. Magn. Mater.* **368**, 75 (2014).
- [40] Y. Hirayama, A. Panda, T. Ohkubo, and K. Hono, High coercivity Sm₂Fe₁₇N₃ submicron size powder prepared by polymerized-complex and reduction-diffusion process, *Scr. Mater.* **120**, 27 (2016).
- [41] J. Fliegans, *Coercivity of NdFeB-based sintered permanent magnets : experimental and numerical approaches*, Theses, Université Grenoble Alpes (2019).
- [42] Q. Cheng, J. Lin, and M. Su, On synthesis and magnetic properties of Nd(Fe, Mo, Ti)₁₂Z_x (Z=N, H), *J. Alloys Compd.* **280**, 310 (1998).
- [43] T. Oyama, ed., *The Chemistry of Transition Metal Carbides and Nitrides*, 1 (Springer Dordrecht) pp. XXVI, 536.
- [44] T. Wu, S. Cao, M. Kou, Y. Xie, G. Ding, S. Guo, B. Zheng, R. Chen, M. Zhong, and A. Yan, Magnetic performance and microstructure of ndfeb sintered magnet by diffusing Tb₁₀Pr_{90-x}(Cu,Al,Ga)_x alloys, *J. Alloys Compd.* **934**, 167888 (2023).
- [45] J. Tsui, K. Strnat, and J. Schweizer, High magnetic coercivity of neodymium- and didymium-cobalt alloys sintered with Pr and Sm additives, *APL* **21**, 446 (2003).
- [46] C. Zhou and F. E. Pinkerton, Magnetic properties of Ce-Nd-Fe-Mo alloys and their nitrides, *J. Magn. Magn. Mater.* **369**, 127 (2014).
- [47] G. Gkouzia, D. Günzing, R. Xie, T. Weßels, A. Kovács, A. T. N'Diaye, M. Major, J. P. Palakkal, R. E. Dunin-Borkowski, H. Wende, H. Zhang, K. Ollefs, and L. Alff, Element-specific study of magnetic anisotropy and hardening in SmCo_{5-x}Cu_x thin films, *Inorg. Chem.* **62**, 16354 (2023), pMID: 37739403.
- [48] K. Suresh, R. Gopalan, A. Singh, G. Bhikshamaiah, V. Chandrasekaran, and K. Hono, Coercivity of Sm(Co_{0.9}Cu_{0.1})_{4.8} melt-spun ribbons, *J. Alloys Compd.* **436**, 358 (2007).
- [49] J. Téllez-Blanco, R. Grössinger, and R. Sato Turtelli, Structure and magnetic properties of SmCo_{5-x}Cu_x alloys, *J. Alloys Compd.* **281**, 1 (1998).
- [50] M. D. Kuz'min, K. P. Skokov, I. Radulov, C. A. Schwöbel, S. Foro, W. Donner, M. Werwiński, J. Rusz, E. Delczeg-Czirjak, and O. Gutfleisch, Magnetic anisotropy of La₂Co₇, *J. Appl. Phys.* **118**, 053905 (2015).
- [51] M. Q. Huang, S. G. Sankar, W. E. Wallace, M. E. McHenry, Q. Chen, and B. M. Ma, Structure and magnetic properties of RCo_{7-x}Zr_x (R=Y, Gd, Nd, or Ho, x=0-0.8), *J. Appl. Phys.* **87**, 5305 (2000).
- [52] M. T. Onyszczyk, T. N. Lamichhane, S. L. Bud'ko, P. C. Canfield, and A. Palasyuk, Structural and magnetic properties of the CeCo₅-CeZn₅ solid solution and potential improvements upon iron substitution, *J. Magn. Magn. Mater.* **482**, 192 (2019).
- [53] Y. Wong, H. Chang, Y. Lee, W. Chang, C. Chiu, and C. Mo, Coercivity enhancement of thicker sintered ndfeb magnets by grain boundary diffusion with low-melting Tb_{75-x}Ce_xCu₂₅ (x=0-45) alloys, *J. Magn. Magn. Mater.* **515**, 167287 (2020).
- [54] W. Silva, N. Ferreira, J. Soares, R. da Silva, and M. Macêdo, Investigation of structural and magnetic properties of nanocrystalline mn-doped SrFe₁₂O₁₉ prepared by proteic sol-gel process, *J. Magn. Magn. Mater.* **395**, 263 (2015).
- [55] S. Katlakunta, S. S. Meena, S. Srinath, M. Bououdina, R. Sandhya, and K. Praveena, Improved magnetic properties of Cr³⁺ doped SrFe₁₂O₁₉ synthesized via microwave hydrothermal route, *Mater. Res. Bull.* **63**, 58 (2015).
- [56] S. Chawla, S. Meena, P. Kaur, R. Mudsainiyan, and S. Yusuf, Effect of site preferences on structural and magnetic switching properties of CO-Zr doped strontium hexaferrite SrCo_xZr_xFe_(12-2x)O₁₉, *J. Magn. Magn. Mater.* **378**, 84 (2015).
- [57] R. Alange, P. P. Khirade, S. D. Birajdar, A. V. Humbe, and K. Jadhav, Structural, magnetic and dielectrical

- properties of Al–Cr Co-substituted m-type barium hexaferrite nanoparticles, *J. Mol. Struct.* **1106**, 460 (2016).
- [58] J. Lee, E. J. Lee, T.-Y. Hwang, J. Kim, and Y.-H. Choa, Anisotropic characteristics and improved magnetic performance of Ca–La–Co-substituted strontium hexaferrite nanomagnets, *Sci. Rep.* **10**, 15929 (2020).
- [59] M. R. Rehman, M. A. Akram, and I. H. Gul, Improved electrical properties of strontium hexaferrite nanoparticles by Co^{2+} substitutions, *ACS Omega* **7**, 43432 (2022).
- [60] K. Lee, Y.-M. Kang, and S.-I. Yoo, Effects of La-Co substitution and post-annealing on the magnetic properties of SrM hexaferrites (2022).
- [61] M. L. Ghimire, D. L. Kunwar, J. N. Daha, S. Dipesh Neupane, Sunghyun Yoon, and R. Mishra, Co-doped rare-earth (La, Pr) and Co-Al substituted m-type strontium hexaferrite: Structural, magnetic, and mossbauer spectroscopy study, *MSA* **11**, 474 (2020).
- [62] K. Aldealat, B. Aladerah, A. Obeidat, and M. Gharaibeh, First-principles study of electronic structure and magnetic properties of L10-ordered FeNi, FePd, and FePt alloys, *Heliyon* **7**, e08639 (2021).
- [63] L. Luo, N. Anuniwat, N. Dao, Y. Cui, S. A. Wolf, and J. Lu, Magneto-transport and domain wall scattering in epitaxy L1 MnAl thin film, *J. Appl. Phys.* **119**, 103902 (2016).
- [64] R. S. Azis, S. Sulaiman, I. R. Ibrahim, A. Zakaria, J. Hassan, N. N. C. Muda, R. Nazlan, N. M. Saiden, Y. W. Fen, M. S. Mustafa, and K. A. Matori, Influence of pH adjustment parameter for sol–gel modification on structural, microstructure, and magnetic properties of nanocrystalline strontium ferrite, *Nanoscale Res. Lett* **13**, 160 (2018).
- [65] Y. He, P. Adler, S. Schneider, I. Soldatov, Q. Mu, H. Borrmann, W. Schnelle, R. Schaefer, B. Rellinghaus, G. H. Fecher, and C. Felser, Intrinsic magnetic properties of a highly anisotropic rare-earth-free Fe_2P -based magnet, *Adv. Funct. Mater.* **32**, 2107513 (2022).
- [66] K. J. Strnat and R. M. Strnat, Rare earth-cobalt permanent magnets, *J. Magn. Magn. Mater.* **100**, 38 (1991).
- [67] A. Kovacs, J. Fischbacher, M. Gusenbauer, H. Oezelt, H. C. Herper, O. Y. Vekilova, P. Nieves, S. Arapan, and T. Schrefl, Computational design of rare-earth reduced permanent magnets, *Eng.* **6**, 148 (2020).
- [68] J. Luo, Y. Xu, and H. Mao, Magnetic and microwave absorption properties of rare earth ions (Sm^{3+} , Er^{3+}) doped strontium ferrite and its nanocomposites with polypyrrole, *J. Magn. Magn. Mater.* **381**, 365 (2015).
- [69] P. Nieves, S. Arapan, J. Maudes-Raedo, R. Marticorena-Sánchez, N. Del Brío, A. Kovacs, C. Echevarria-Bonet, D. Salazar, J. Weischenberg, H. Zhang, O. Vekilova, R. Serrano-López, J. Barandiaran, K. Skokov, O. Gutfleisch, O. Eriksson, H. Herper, T. Schrefl, and S. Cuesta-López, Database of novel magnetic materials for high-performance permanent magnet development, *Comput. Mater. Sci.* **168**, 188 (2019).
- [70] Z. Li, B. Shen, M. Zhang, F. Hu, and J. Sun, Substitution of ce for nd in preparing $\text{R}_2\text{Fe}_{14}\text{B}$ nanocrystalline magnets, *J. Alloys Compd.* **628**, 325 (2015).
- [71] M. A. Susner, B. S. Conner, B. I. Saporov, M. A. McGuire, E. J. Crumlin, G. M. Veith, H. Cao, K. V. Shanavas, D. S. Parker, B. C. Chakoumakos, and B. C. Sales, 2flux growth and characterization of Ce-substituted $\text{Nd}_2\text{Fe}_{14}\text{B}$ single crystals, *J. Magn. Magn. Mater.* **434**, 1 (2017).
- [72] K. Kobayashi, K. Urushibata, T. Matsushita, S. Sakamoto, and S. Suzuki, Magnetic properties and domain structures in Nd–Fe–B sintered magnets with tb additive reacted and diffused from the sample surface, *J. Alloys Compd.* **615**, 569 (2014).
- [73] S. ying Zhang, Z. gang Sun, H. wei Zhang, B. shan Han, B. gen Shen, F. R. de Boer, and K. H. J. Buschow, Magnetic properties and magnetic-domain structures of nanocrystalline $\text{Sm}_2\text{Fe}_{14.5}\text{Cu}_{0.5}\text{Ga}_2\text{C}_y$ and $\text{Sm}_2\text{Fe}_{15}\text{Ga}_2\text{C}_{1.0}$ ribbons prepared by melt-spinning, *J. Phys. D* **32**, 2990 (1999).
- [74] X. Fan, S. Guo, K. Chen, R. Chen, D. Lee, C. You, and A. Yan, Tuning ce distribution for high performed Nd-Ce-Fe-B sintered magnets, *J. Magn. Magn. Mater.* **419**, 394 (2016).
- [75] B. Zhou, Y. Liu, S. Li, W. Fan, X. Liao, J. He, H. Yu, and Z. Liu, Phase precipitation and magnetic properties of melt-spun ternary $\text{Gd}_2\text{Fe}_{14}\text{B}$ alloy and advantages of gadolinium substitution in $\text{Y}_2\text{Fe}_{14}\text{B}$ alloy, *J. Rare Earths* **41**, 1058 (2023).
- [76] S. Lee, B. Das, and V. Harris, Magnetic structure of single crystal $\text{Tb}_2\text{Fe}_{14}\text{B}$, *J. Magn. Magn. Mater.* **207**, 137 (1999).
- [77] J. Fischbacher, A. Kovacs, H. Oezelt, M. Gusenbauer, D. Suess, and T. Schrefl, Effective uniaxial anisotropy in easy-plane materials through nanostructuring, *APL* **111**, 192407 (2017).
- [78] X. B. Liu and I. C. Nlebedim, Phase stability and coercivity in $\text{La}_2\text{Fe}_{14}\text{B}$ magnet, *AIP Advances* **13**, 025211 (2023).
- [79] D. Goll, R. Loeffler, J. Herbst, R. Karimi, U. Pflanz, R. Stein, and G. Schneider, High-throughput methods for searching new permanent magnet materials, *IEEE Transactions on Magnetics* **50**, 1 (2014).
- [80] J.-P. Bick, K. Suzuki, E. P. Gilbert, E. M. Forgan, R. Schweins, P. Lindner, C. Kübel, and A. Michels, Exchange-stiffness constant of a Nd-Fe-B based nanocomposite determined by magnetic neutron scattering, *APL* **103**, 122402 (2013).
- [81] T. Ohtani, N. Kato, S. Kojima, K. Kojima, Y. Sakamoto, I. Konno, M. Tsukahara, and T. Kubo, Magnetic properties of Mn-Al-C permanent magnet alloys, *IEEE Transactions on Magnetics* **13**, 1328 (1977).
- [82] E. A. Nesbitt, New permanent magnet materials containing rare-earth metals., *J. Appl. Phys.*, 40: 1259-65 (Mar. 1, 1969). 10.1063/1.1657135 (1969).
- [83] N. Inaba and M. Futamoto, Exchange stiffness constants of CoCr-alloy thin films, *J. Magn. Magn. Mater.* **226-230**, 1014 (2001), proceedings of the International Conference on Magnetism (ICM 2000).
- [84] T. Ben Ghzaïel, W. Dhaoui, A. Pasko, and F. Mazaleyrat, Effect of non-magnetic and magnetic trivalent ion substitutions on BaM-ferrite properties synthesized by hydrothermal method, *J. Alloys Compd.* **671**, 245 (2016).
- [85] E. H. Frei, S. Shtrikman, and D. Treves, Critical size and nucleation field of ideal ferromagnetic particles, *Phys. Rev.* **106**, 446 (1957).
- [86] G. Herzer, Grain size dependence of coercivity and permeability in nanocrystalline ferromagnets, *IEEE Transactions on Magnetics* **26**, 1397 (1990).

- [87] R. Skomski and J. Coey, Magnetic anisotropy — how much is enough for a permanent magnet?, *Scr. Mater.* **112**, 3 (2016).
- [88] H. Kronmüller, Theory of nucleation fields in inhomogeneous ferromagnets, *physica status solidi (b)* **144**, 385 (1987).
- [89] F. E. Pinkerton and C. D. Fuerst, Temperature dependence of coercivity in melt-spun and die upset neodymium-iron-boron, *J. Appl. Phys.* **67**, 4753 (1990).
- [90] J. Herbst and J. Croat, Neodymium-iron-boron permanent magnets, *J. Magn. Magn. Mater.* **100**, 57 (1991).
- [91] R. Alben, J. J. Becker, and M. C. Chi, Random anisotropy in amorphous ferromagnets, *J. Appl. Phys.* **49**, 1653 (2008).
- [92] O. Akdogan, W. Li, B. Balasubramanian, D. J. Sellmyer, and G. C. Hadjipanayis, Effect of exchange interactions on the coercivity of SmCo_5 nanoparticles made by cluster beam deposition, *Adv. Funct. Mater.* **23**, 3262 (2013).
- [93] G. Herzer, Soft magnetic nanocrystalline materials, *Scr. Mater.* **33**, 1741 (1995), proceedings of an Acta Metallurgica Meeting on Novel Magnetic Structures and Properties.
- [94] G. Herzer, Grain size dependence of coercivity and permeability in nanocrystalline ferromagnets, *IEEE Transactions on Magnetics* **26**, 1397 (1990).
- [95] R. Fischer, T. Schrefl, H. Kronmüller, and J. Fidler, Grain-size dependence of remanence and coercive field of isotropic nanocrystalline composite permanent magnets, *J. Magn. Magn. Mater.* **153**, 35 (1996).
- [96] R. Ramesh, G. Thomas, and B. M. Ma, Magnetization reversal in nucleation controlled magnets. ii. effect of grain size and size distribution on intrinsic coercivity of Fe-Nd-B magnets, *J. Appl. Phys.* **64**, 6416 (1988).
- [97] S. Bance, B. Seebacher, T. Schrefl, L. Exl, M. Winkelhofer, G. Hrkac, G. Zimanyi, T. Shoji, M. Yano, N. Sakuma, M. Ito, A. Kato, and A. Manabe, Grain-size dependent demagnetizing factors in permanent magnets, *J. Appl. Phys.* **116**, 233903 (2014).
- [98] F. Pedregosa, G. Varoquaux, A. Gramfort, V. Michel, B. Thirion, O. Grisel, M. Blondel, P. Prettenhofer, R. Weiss, V. Dubourg, *et al.*, Scikit-learn: Machine learning in python, *J. Mach. Learn. Res.* **12**, 2825 (2011).
- [99] D. P. Kingma and J. Ba, Adam: A method for stochastic optimization (2017), arXiv:1412.6980 [cs.LG].
- [100] M. Abadi, A. Agarwal, P. Barham, E. Brevdo, Z. Chen, C. Citro, G. S. Corrado, A. Davis, J. Dean, M. Devin, S. Ghemawat, I. Goodfellow, A. Harp, G. Irving, M. Isard, Y. Jia, R. Jozefowicz, L. Kaiser, M. Kudlur, J. Levenberg, D. Mané, R. Monga, S. Moore, D. Murray, C. Olah, M. Schuster, J. Shlens, B. Steiner, I. Sutskever, K. Talwar, P. Tucker, V. Vanhoucke, V. Vasudevan, F. Viégas, O. Vinyals, P. Warden, M. Wattenberg, M. Wicke, Y. Yu, and X. Zheng, TensorFlow: Large-scale machine learning on heterogeneous systems (2015), software available from tensorflow.org.
- [101] F. Chollet *et al.*, Keras (2015).
- [102] C. J. S. Leo Breiman, Jerome Friedman and R. Olshen, *Classification and Regression Trees* (Chapman and Hall/CRC, 1984).
- [103] G. Kresse and J. Furthmüller, Efficient iterative schemes for ab initio total-energy calculations using a plane-wave basis set, *Phys. Rev. B* **54**, 11169 (1996).
- [104] G. Kresse and J. Furthmüller, Efficiency of ab-initio total energy calculations for metals and semiconductors using a plane-wave basis set, *Comput. Mater. Sci.* **6**, 15 (1996).
- [105] J. P. Perdew, K. Burke, and M. Ernzerhof, Generalized gradient approximation made simple, *Phys. Rev. Lett.* **77**, 3865 (1996).
- [106] P. E. Blöchl, Projector augmented-wave method, *Phys. Rev. B* **50**, 17953 (1994).
- [107] S. L. Duarev, G. A. Botton, S. Y. Savrasov, C. J. Humphreys, and A. P. Sutton, Electron-energy-loss spectra and the structural stability of nickel oxide: An LSDA+U study, *Phys. Rev. B* **57**, 1505 (1998).
- [108] O. Isnard, W. B. Yelon, S. Miraglia, and D. Fruchart, Neutron-diffraction study of the insertion scheme of hydrogen in $\text{Nd}_2\text{Fe}_{14}\text{B}$, *J. Appl. Phys.* **78**, 1892 (1995).
- [109] H. Oesterreicher, F. Spada, and C. Abache, Anisotropic and high magnetization rare earth transition metal compounds containing metalloids, *Mater. Res. Bull.* **19**, 1069 (1984).
- [110] V. I. Anisimov, J. Zaanen, and O. K. Andersen, Band theory and mott insulators: Hubbard U instead of Stoner I, *Phys. Rev. B* **44**, 943 (1991).
- [111] C. Bhandari and D. Paudyal, Giant magnetic and optical anisotropy in cerium-substituted M-type strontium hexaferrite driven by 4f electrons, *Phys. Rev. Appl.* **20**, 024016 (2023).
- [112] C. Bhandari, M. E. Flatté, and D. Paudyal, Enhanced magnetic anisotropy in lanthanum M-type hexaferrites by quantum-confined charge transfer, *Phys. Rev. Mater.* **5**, 094415 (2021).
- [113] C. Bhandari and D. Paudyal, Enhancing stability and magnetism of ThMn_{12} -type cerium-iron intermetallics by site substitution, *Phys. Rev. Res.* **4**, 023012 (2022).
- [114] M. Sagawa, S. Fujimura, H. Yamamoto, Y. Matsuura, and S. Hirosawa, Magnetic properties of rare-earth-iron-boron permanent magnet materials, *J. Appl. Phys.* **57**, 4094 (1985).
- [115] U. von Barth and L. Hedin, A local exchange-correlation potential for the spin polarized case. i, *J. Phys. C: Solid State Phys.* **5**, 1629 (1972).
- [116] D. Pashov, S. Acharya, W. R. Lambrecht, J. Jackson, K. D. Belashchenko, A. Chantis, F. Jamet, and M. van Schilfgaarde, Questaal: A package of electronic structure methods based on the linear muffin-tin orbital technique, *Comput. Phys. Comm.* **249**, 107065 (2020).
- [117] M. van Schilfgaarde and V. P. Antropov, First-principles exchange interactions in Fe, Ni, and Co, *J. Appl. Phys.* **85**, 4827 (1999).
- [118] A. Liechtenstein, M. Katsnelson, V. Antropov, and V. Gubanov, Local spin density functional approach to the theory of exchange interactions in ferromagnetic metals and alloys, *J. Magn. Magn. Mater.* **67**, 65 (1987).
- [119] Weiss, Pierre, L'hypothèse du champ moléculaire et la propriété ferromagnétique, *J. Phys. Theor. Appl.* **6**, 661 (1907).
- [120] S. Tiaablikov, *Methods in the Quantum Theory of Magnetism* (Springer US, 2013).
- [121] D. Haskel, J. C. Lang, Z. Islam, A. Cady, G. Srajer, M. van Veenendaal, and P. C. Canfield, Atomic origin of magnetocrystalline anisotropy in $\text{Nd}_2\text{Fe}_{14}\text{B}$, *Phys. Rev. Lett.* **95**, 217207 (2005).
- [122] A. K. Pathak, M. Khan, K. A. Gschneidner Jr., R. W. McCallum, L. Zhou, K. Sun, K. W. Dennis, C. Zhou,

- F. E. Pinkerton, M. J. Kramer, and V. K. Pecharsky, Cerium: An unlikely replacement of dysprosium in high performance Nd–Fe–B permanent magnets, *Adv. Mater.* **27**, 2663 (2015).
- [123] T. Sasaki, T. Ohkubo, Y. Takada, T. Sato, A. Kato, Y. Kaneko, and K. Hono, Formation of non-ferromagnetic grain boundary phase in a Ga-doped Nd-rich Nd–Fe–B sintered magnet, *Scripta Materialia* **113**, 218 (2016).
- [124] P. Larson, I. I. Mazin, and D. A. Papaconstantopoulos, Calculation of magnetic anisotropy energy in SmCo₅, *Phys. Rev. B* **67**, 214405 (2003).
- [125] M. Sakurai, S. Wu, X. Zhao, M. C. Nguyen, C.-Z. Wang, K.-M. Ho, and J. R. Chelikowsky, Magnetocrystalline anisotropy in YCo₅ and ZrCo₅ compounds from first-principles real-space pseudopotentials calculations, *Phys. Rev. Mater.* **2**, 084410 (2018).